



Synthesis of Fe@Ni nanoparticles-modified graphene/epoxy composites with enhanced microwave absorption performance

Bin Zhang¹ · Jun Wang^{1,2} · Haoyuan Tan³ · Xiaogang Su¹ · Siqi Huo¹ · Shuang Yang^{2,4} · Wei Chen¹ · Junpeng Wang⁵

Received: 9 October 2017 / Accepted: 14 November 2017 / Published online: 18 November 2017
© Springer Science+Business Media, LLC, part of Springer Nature 2017

Abstract

High performance microwave absorber consisting of Fe@Ni nanoparticles (NPs) modified reduced graphene oxide (RGO) and epoxy resin was successfully prepared. Fe@Ni NPs obtained via electroless plating method could be simply anchored on the surface of RGO sheets because of its high surface area, as well as residual organic groups of RGO. The crystal/micro-structure and magnetic properties of as-synthesized samples were subsequently analyzed by XRD, SEM, TEM, XPS and VSM, while electromagnetic properties were tested by vector network analyzer. The synergistic effect between graphene and Fe@Ni NPs generated suitable impedance match and strong microwave attenuation ability which lead to excellent microwave absorption property. The optimal reflection loss (RL) calculated from measured electromagnetic parameters can reach up to -22.7 dB at 14.9 GHz with a layer thickness of 2 mm. Moreover, RL values < -10 dB is found to be 5.5 GHz within 12.5–18 GHz, almost covering the entire Ku band. It's convincing that the as-synthesized composites are potential candidates for high-performance lightweight microwave absorbers.

1 Introduction

In the past decades, the innovations of science and technology have largely improved our daily life, especially the benefits derived from electromagnetic (EM) wave technology such as the wireless communication, broadcast, radar, etc [1, 2]. However, accompany with massive use of electric equipment in commerce and military, issue of EM wave pollution raises, which interferes electrical device operation and harms biological system under long-time microwave exposure [3, 4]. Therefore, considerable researches have been carried out to design and synthesize high performance

microwave absorbing materials to eliminate those adverse EM waves, such as carbonyl iron, ferrite, carbon black, carbon fibers, conducting polymers and so on [5–9].

An ideal microwave absorber should exhibit thin thickness, light weight, broad absorption bandwidth and strong attenuation ability simultaneously [10]. In order to achieve these objectives, the microwave absorber must show well impedance match and extensive attenuation ability. This means reflection of incident microwave onto the surface of absorber should be as minimal as possible, and the EM energy inside the absorber should be converted and dissipated efficiently. Traditional ferrites have been widely used as microwave absorbing materials because of its acceptable magnetic loss, stability, low price and easy-to-get feature. The permeability of both spinel and hexagonal ferrites decreases dramatically with increasing frequency because of the Snoek's limit, leading to poor microwave absorption property which restricts their applications [11, 12]. While metallic magnetic materials can conquer those problems and retain high permeability at high frequency, which is more suitable as microwave absorbing materials considering its higher saturation magnetization. Wen et al. [13] fabricated flake-assembled cobalt absorber through liquid reduction method and the peak value was up to -77.29 dB with a layer thickness of 1.5 mm, while the effective absorption bandwidth exceeding -10 dB seemed a little narrow (only

✉ Jun Wang
wgdfp@whut.edu.cn

¹ School of Materials Science and Engineering, Wuhan University of Technology, Wuhan 430070, China

² Institute of Advanced Material Manufacturing Equipment and Technology, Wuhan University of Technology, Wuhan 430070, China

³ Department of Mechanical Engineering, University College London, Torrington Place, London WC1E 7JE, UK

⁴ School of Mechanical and Electronic Engineering, Wuhan University of Technology, Wuhan 430070, China

⁵ Aerospace Science and Industry Wuhan Magnetolectric Co., Ltd, Wuhan 430070, China

3.6 GHz). The narrow bandwidth limits its application due to the single loss mechanism and impedance mismatch. Zhang et al. [14] synthesized carbon-coated Ni nanocapsules via modified arc-discharge method. The average size of Ni nanoparticles (NPs) was about 20 nm less than the skin depth, so that the metallic magnetic Ni NPs could avert the eddy current phenomenon and the maximum reflection loss (RL) could reach up to -32 dB. The combination of these two loss mechanism materials may be an admissible choice to acquire excellent microwave absorbers [15].

Carbon-based materials, typically graphene, have recently received wide attention and interest for its unique physical and chemical properties with wide application such as electronics, optics, solar energy harvesting, batteries, supercapacitors, fuel cells, charge-storage devices and so on [16, 17]. Graphene can be prepared through various methods, such as mechanical exfoliation, thermal exfoliation of graphite oxide, liquid-phase exfoliation, supercritical CO₂ processing technique and chemical reduction of GO [18]. Reduced graphene oxide (RGO) have been proved to be potential microwave absorbing materials in 2011 [19], though the peak value was higher than -10 dB. Ulteriorly, Zhang et al. prepared 3D free-standing graphene foam via self-assembly method, which possessed air-similar density and amazing microwave absorbing performance [20]. With the help of its special structure, magnetic NPs are easily anchored on the surface of graphene nanosheets to synthesize excellent EM wave absorbers. Wang et al. [21] synthesized surface modified Fe₅₀Ni₅₀-RGO using a wet chemical procedure with a maximum RL up to -23.9 dB. Zhu et al. [22] produced RGO-Ni composites through a microwave-assisted heating approach and its maximum RL was -42 dB with an effective absorption bandwidth of nearly 6 GHz. Through those results above, it can be speculated that the incorporation of graphene with metallic magnetic NPs is expected to achieve ideal microwave absorption performance.

Concerning the past researches, microwave absorption performance of Fe@Ni NPs modified RGO/epoxy composites have not been reported. In the present work, the combination of lightweight dielectric graphene and magnetic Fe@Ni NPs provides a facile approach to achieve high-performance microwave absorbers. The absorption performance can be tuned by weight ratio of RGO to Fe@Ni NPs with better impedance match and enhanced microwave attenuation. Based on the microstructure characteristic, EM properties and theoretical calculations, a conceivable mechanism has been proposed to explain the enhanced microwave absorption performance.

2 Experimental section

2.1 Preparation of core-shell Fe@Ni nanoparticles

All reagents were analytical grade without further purification and obtained commercially, and distilled water was used throughout the whole experiment. Core-shell Fe@Ni NPs were synthesized by electroless plating method [23]. Nickel sulfate hexahydrate (NiSO₄·6H₂O) was the nickel source, and hydrazine hydrate (N₂H₄·H₂O, 85%) was used as reducing agent. The reduction process was sketched as below:



0.4 g acetone pretreated Fe NPs, 5.26 g NiSO₄·6H₂O, 10 g C₄H₄KNaO₆·4H₂O and 0.1 mg CH₄N₂S were dispersed in 200 mL ethanol solution under ultrasonic treatment for 0.5 h to obtain a dark gray solution. Then, alkaline reductants containing 12 g N₂H₄·H₂O were injected into above solution until pH value up to 11. The mixture was under vigorous mechanical stirring at 90 °C for 2 h. With sufficient centrifugation and abstersion, the black product was finally synthesized.

2.2 Synthesis of Fe@Ni functionalized RGO (GFN) composites

Detailed preparation of RGO were described in [24, 25], which possess large lateral dimension and perfect conductivity, improving the microwave absorption property. In addition, the defects and residual groups during the oxidation-reduction process may induce the formation of polarization centers, leading to enhanced microwave absorption [20]. The GFN composites was prepared based on electrostatic attraction. Fe@Ni NPs was added into RGO solution (1 mg/mL) and sonicated for 1.0 h to obtaining the product used in next step.

2.3 Characterization

The crystal structural of samples was characterized by X-ray diffraction (XRD, Bruker D8 Advance diffractometer). The morphology and microstructure were conducted by scanning electron microscopy (SEM, Zeiss Merlin Compact) and transmission electron microscope (TEM, JEOL-2100F), and element mapping distribution was recorded on energy dispersive X-ray spectrometry (EDS, Oxford X-50MAX). Element binding energy was acquired by X-ray photoelectron spectrometer (XPS, Thermo Scientific K-Alpha) and magnetic property were analyzed by vibrating sample magnetometry (VSM, YinPu, JDAW-2000D).

Scattering parameters were measured by vector network analyzer (VNA, Agilent N5247A) and coaxial sample holder (Agilent 85051-60007) within frequency of 1–18 GHz.

Calibration of VNA was in the same frequency range: a power of +5 dBm was set to increase the dynamic range of measurements and an IF bandwidth of 300 Hz was set to increase the accuracy of the measurements. On the basis of Nicolson–Ross–Weir (NRW) method [26], EM parameters were obtained through the materials parameters software (Agilent 85071E). Different formulations of GFN/epoxy composites having epoxy: Fe@Ni: RGO weight ratios of 100:2:1, 100:5:1, 100:10:1 and 100:10:0 were prepared for EM test, labeled as GFN-2, GFN-5, GFN-10 and GFN-0 respectively. Those samples were prepared by solution processing described in our previous research [21].

3 Results and discussion

The crystal structure and chemical components of Fe@Ni and GFN samples were characterized by XRD, shown in Fig. 1. Focusing on curve (a), peaks located at $2\theta = 44.6^\circ$ and 65° can be identified as body-centered cubic Fe (JCPDS No. 06-0696), while the other peaks located at $2\theta = 44.5^\circ$, 51.8° and 76.4° exhibit a typical diffraction pattern of face-centered cubic Ni (JCPDS No. 65-2865), corresponding to (111), (200) and (220) planes, respectively [27, 28]. It's obvious that curve (a–d) show similar diffraction peaks and the slightly weakened intensity of Fe and Ni peaks may originate from the covering of Fe@Ni by RGO sheets. In addition, curve (b) exhibits a weak peak at around 20° – 30° , a typical pattern for carbon structure of graphene [29]. With increasing addition of Fe@Ni particles, the well-arranged stacking structure of graphene sheets is broke and collapsed so that the characteristic peak disappears in curve (c, d),

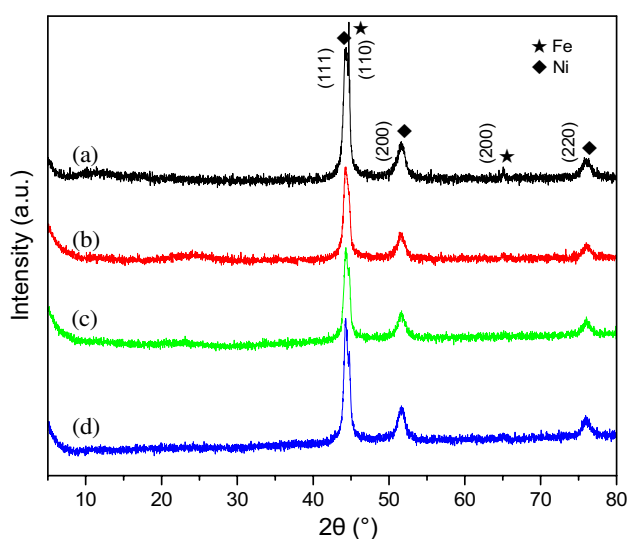


Fig. 1 XRD patterns of (a) Fe@Ni and (b–d) GFN particles with different weight ratio of Fe@Ni to RGO (2:1, 5:1 and 10:1)

indicating the successful anchoring of Fe@Ni NPs on RGO sheets.

The elemental components of GO, RGO and GFN composites were further investigated by XPS. Figure 2a, b show general surveys of GO/RGO and GFN powders, respectively. The C/O atom ratio of GO changes significantly from 62.8%/37.2–81.7%/18.3% of RGO, indicating the successful reduction with HI–AcOH as reductant. With further analysis in Fig. 2c, C 1s spectrum of GO is deconvoluted to four characteristic peaks, including C–C/C=C (284.6 eV), C–OH (285.6 eV), C–O (286.7 eV) and C=O (288.6 eV). After HI–AcOH reduction, the peaks of oxygen functional groups decrease apparently even disappear but still exist, demonstrating the favorable reduction of GO and the existence of residual oxygenate groups [30]. The C/O atomic ratio increases dramatically manifesting a successful reduction of GO. While for GFN powders in Fig. 2b, an interesting phenomenon occurs, the C/O atomic ratio decrease to some extent compared with RGO, possibly because of the oxidation of Fe or Ni during the dehydration process. However, the typical Fe 2p and Ni 2p signals reveal that Fe@Ni NPs have been decorated on graphene sheets. As depicted in followed figures, binding energy appears at 724.6 and 710.8 eV is assigned to the Fe $2p_{1/2}$ signal and Fe $2p_{3/2}$ level [31], the binding energy peak at 855.1 eV for Ni $2p_{3/2}$ and satellite peak at 860.7 eV further supported the existence of Ni [32]. All XPS results are in accordance with XRD consequence, declaring the assembly of Fe@Ni NPs on RGO sheets ulteriorly.

Figure 3 exhibits the magnetic hysteresis loops of Fe@Ni, Fe@Ni NPs and GFN composites with an applied magnetic field (± 6000 Oe) at ambient temperature. The saturation magnetization of commercial Fe and as-synthesized Fe@Ni NPs are 124.3 and 98.8 emu/g, respectively. Generally speaking, the magnetic properties of crystalline materials are markedly higher than amorphous materials [33], so that these synthesized particles in the present work exhibit lower magnetic characteristics than the crystalline Fe NPs. In addition, compared with curve (b) and curve (c–e), the lower M_s of GFN powders is on account of the existence of nonmagnetic RGO sheets. Different weight ratios of Fe@Ni NPs to RGO give rise to diverse magnetic properties. It's obvious that higher Fe@Ni content in the GFN powders will result in higher saturation magnetization (M_s) and lower coercive force (H_c). The M_s of the GFN powders decreases from 87.6 to 21.1 emu/g as Fe@Ni/RGO weight ratio increases from 2:1 to 10:1, while the H_c reduces scarcely. Moreover, the Fe@Ni NPs and GFN composites show soft ferromagnetic behavior with a very small H_c in the range of 45–50 Oe. The inset digital photograph in Fig. 3 directly shows that the GFN particles dispersed in alcohol solution can be promptly attracted and gathered around a magnet, indicating the successful assembly of Fe@Ni NPs on RGO sheets.

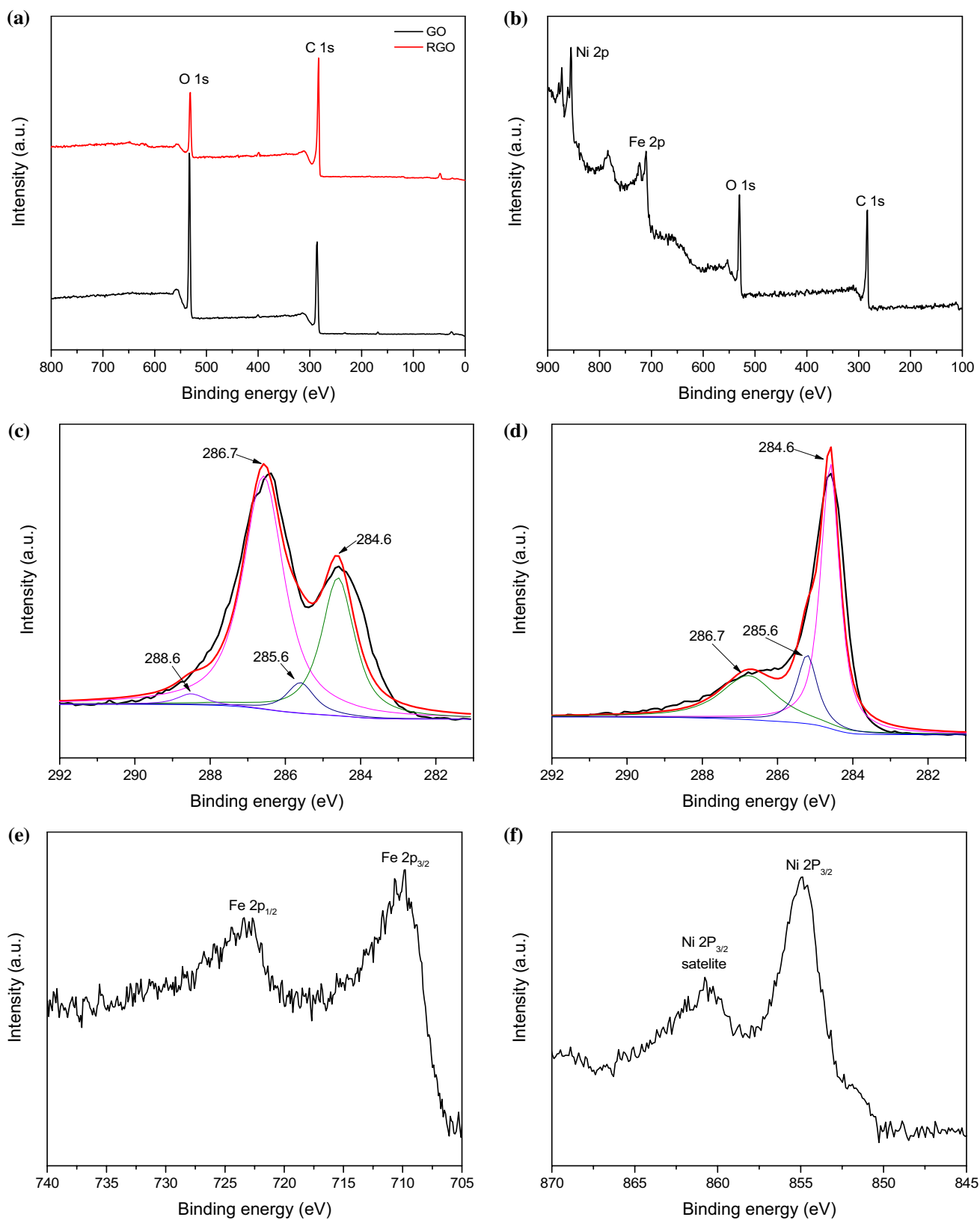


Fig. 2 XPS spectra survey of **a** GO, RGO and **b** GFN composites; C 1s spectrum of **c** GO and **d** RGO; **e** Fe 2p spectrum and **f** Ni 2p spectrum of GFN composites

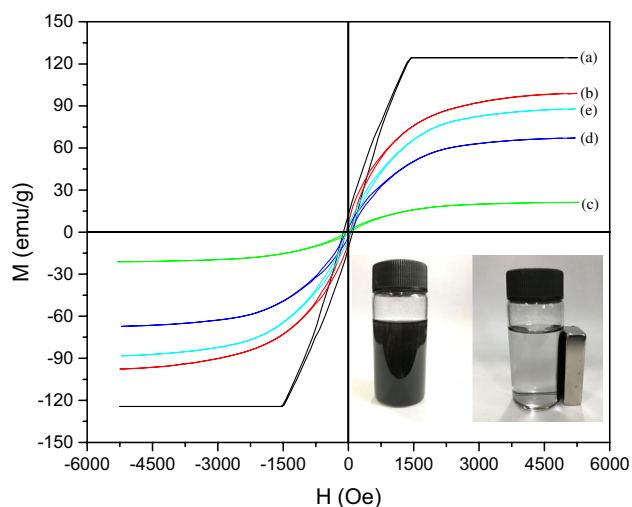


Fig. 3 Magnetization hysteresis loops of (a) commercial Fe NPs, (b) Fe@Ni NPs and (c–e) GFN powders with different weight ratio of Fe@Ni to RGO (2:1, 5:1 and 10:1)

The morphology of Fe@Ni NPs and GFN composites have been recorded by SEM and TEM. Those commercial Fe NPs exhibit spheroidal shape and possess general diameter of 60–100 nm. As shown in Fig. 4a, Fe NPs are almost entirely covered by Ni, while the black dots in red circle suggest incomplete covering. In order to get more accurate observation, TEM has been conducted that the Fe core is completely coated by Ni shell with layer thickness of about 8 nm (Fig. 4b). Due to high surface area and electronegative oxygen-containing groups on RGO sheets, Fe@Ni NPs can be attracted and attached on both sides of RGO sheets. As Fe@Ni NPs loading is low, graphene sheets are not completely filled with Fe@Ni NPs and large area of wrinkled graphene sheets expose on conducting substrate in Fig. 4c. By increasing the dosage of Fe@Ni NPs, these particles will occupy more surface of RGO sheets (Fig. 4d), which is beneficial to hinder the aggregation and enhance the conductive networks. Furthermore, the Fe@Ni NPs distribution is clearly depicted by element mapping diagram in Fig. 4e, f, confirming the high proportion covering of Fe@Ni NPs on RGO layers.

The EM parameters of Fe@Ni/epoxy composites and GFN/epoxy composites are mainly expressed by complex permittivity ($\epsilon_r = \epsilon' - j\epsilon''$) and complex permeability ($\mu_r = \mu' - j\mu''$), which are adopted to estimate the microwave absorption performance of as-synthesized absorbing materials. Generally, these real parts are associated with the stored electrical and magnetic energy, while those imaginary parts stand for dissipation of electrical and magnetic energy within an absorber [34]. Figure 5a, b depict the frequency dependence of complex permittivity. ϵ' value of GFN-0 sample is around ~ 4.1 with a tiny fluctuation within 1–18 GHz.

While for those GFN/epoxy samples, the ϵ' values decrease significantly with increasing frequency, because of an increased lagging of the dipole-polarization response with respect to the electrical field variation [35, 36]. It's apparent that all ϵ' values of GFN/epoxy samples are higher than that of Fe@Ni/epoxy samples, owing to the addition of electric conducting graphene sheets though the loading is in fairly low level. With further analysis, the appearance of this phenomenon can be attributed to interfacial polarization. On basis of Maxwell–Wagner–Sillars (MWS) principle [37], or interfacial polarization principle, the diversity between two adjacent materials induces space charge accumulation at their interfaces, leading to the interfacial polarization. Epoxy resin, as the matrix phase, is a polar polymer. Once GFN particles uniformly disperse in epoxy matrix, the interfaces between Fe@Ni/RGO, RGO/epoxy and Fe@Ni/epoxy give rise to more interfacial polarization, which finally result in higher permittivity. While in Fe@Ni/epoxy composites, the interfaces seem limited, hence, a weaker permittivity comes out. Moreover, distinguished from the variation tendency of real parts, ϵ'' of GFN-0 samples retains a constant about 0.21 in 1–12 GHz range, then have a slight rise to 0.41. Analogously, the ϵ'' values of GFN-2, GFN-5 and GFN-10 samples stay around 1.0–1.3, 1.4–1.6 and 2.0–2.4, respectively. Besides, ϵ'' values rise up with increasing loading of GFN particles. This phenomenon can be explained by free electron theory, $\epsilon'' \approx 1/2\pi\epsilon_0 f$ [38]. Owing to the conductive RGO sheets and metallic Fe@Ni NPs, a promoted conductive network generates. Therefore, these GFN/epoxy composites possess higher incremental electrical conductivity, leading to higher ϵ'' values than Fe@Ni/epoxy composites.

The real (μ') and imaginary (μ'') part of complex permeability are plotted in Fig. 5c, d as a function of frequency. For all prepared samples, complex permeability decrease with increasing frequency though variations seem small. Considering that permeability mainly originates from the magnetic Fe@Ni NPs, the increasing Fe@Ni ratio leads to enhanced magnetic properties. However, a peculiar phenomenon which cannot be neglected exists that both μ' and μ'' of GFN-10 composites exceed those of GFN-0 composites occasionally, though they have similar complex permeability with same content of magnetic Fe@Ni NPs. The tiny reinforcement of complex permeability may be ascribed to coupled interaction effect between dielectric graphene sheets and magnetic Fe@Ni NPs. As a rule, magnetic loss is in connection with magnetic hysteresis, domain wall resonance, eddy current effect exchange resonance [39]. Magnetic hysteresis comes from the delay of magnetization vector behind the external magnetic field, which could be neglected because of the present weak applying field. Domain wall resonance usually appears in MHz range, not in current frequency range. As a consequence, these two loss types can be excluded for magnetic loss. When the value of $C_0 = \mu''(\mu')^{-2}f^{-1}$ stabilise

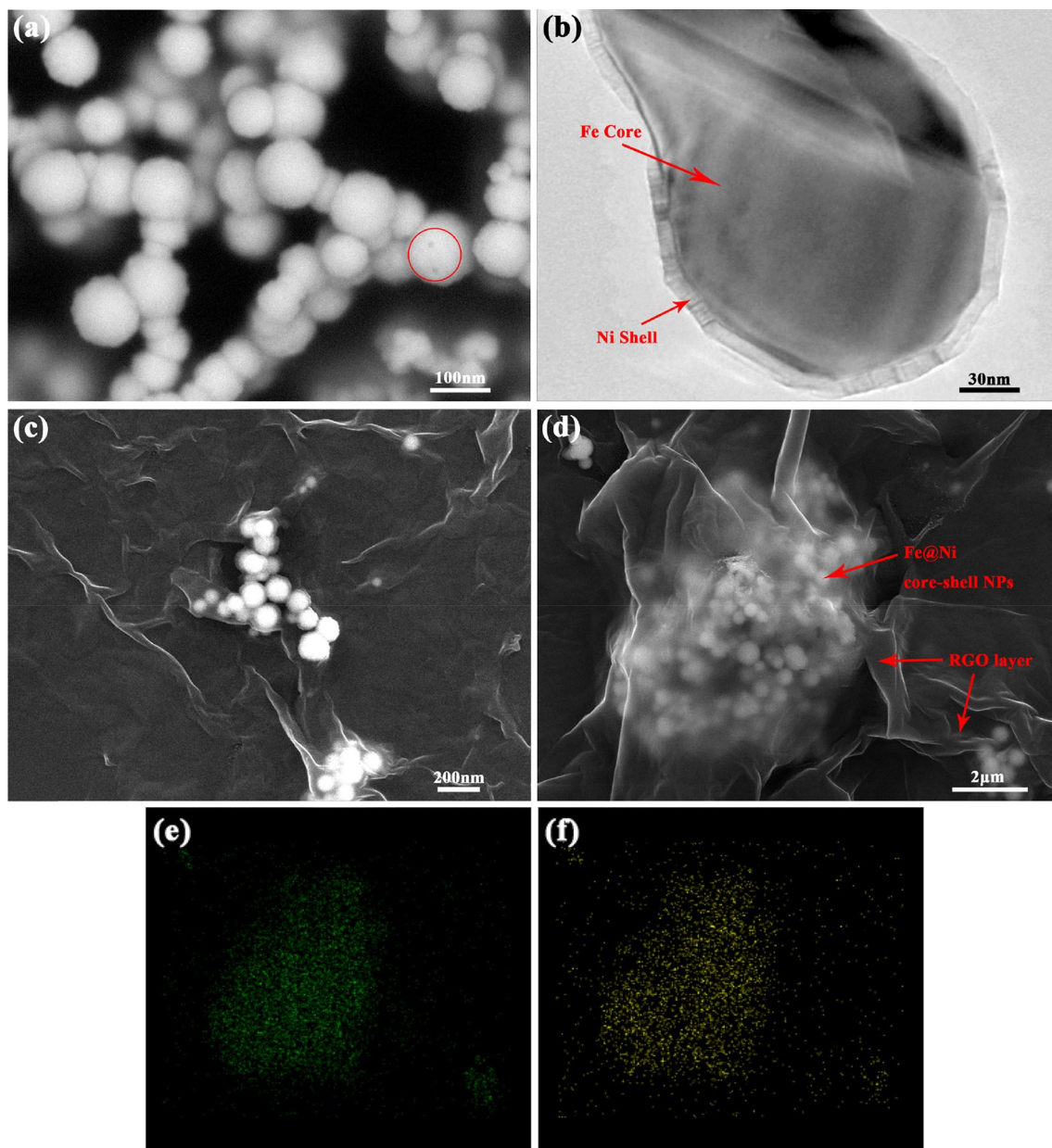


Fig. 4 **a** SEM and **b** TEM image of Fe@Ni NPs, **c**, **d** SEM images of GFN powders, EDS patterns of **e** Ni and **f** Fe element

at a constant, thus magnetic loss originates from the eddy current loss [40]. Figure 6 shows the C_0 - f curves of as-prepared samples, C_0 apparently declines sharply along with frequency variation within 1–10 GHz, indicating the eddy current effect is effectively suppressed because of the nano-sized Fe@Ni NPs. Subsequently, the value of C_0 remains constant in higher frequency, declaring that eddy current effect dominates magnetic loss for microwave absorption.

The microwave absorption performance can be presented by RL values, which are calculated from the measured EM parameters at a given frequency and layer thickness by means of following expressions [41]:

$$Z_{in} = Z_0 \sqrt{\mu_r/\epsilon_r} \tanh(j2\pi f d \sqrt{\mu_r \epsilon_r}/c) \quad (2)$$

$$R_L = 20 \log \left| (Z_{in} - Z_0)/(Z_{in} + Z_0) \right| \quad (3)$$

where f is the microwave frequency, d is the thickness of the absorber and c is the velocity of light in vacuum, Z_{in} is the input impedance of the absorber, Z_0 is the free space characteristic impedance.

Figure 7 shows the relationship of RL, frequency and layer thickness in a three-dimensional pattern. It is seen that thickness and frequency have a significant impact on microwave

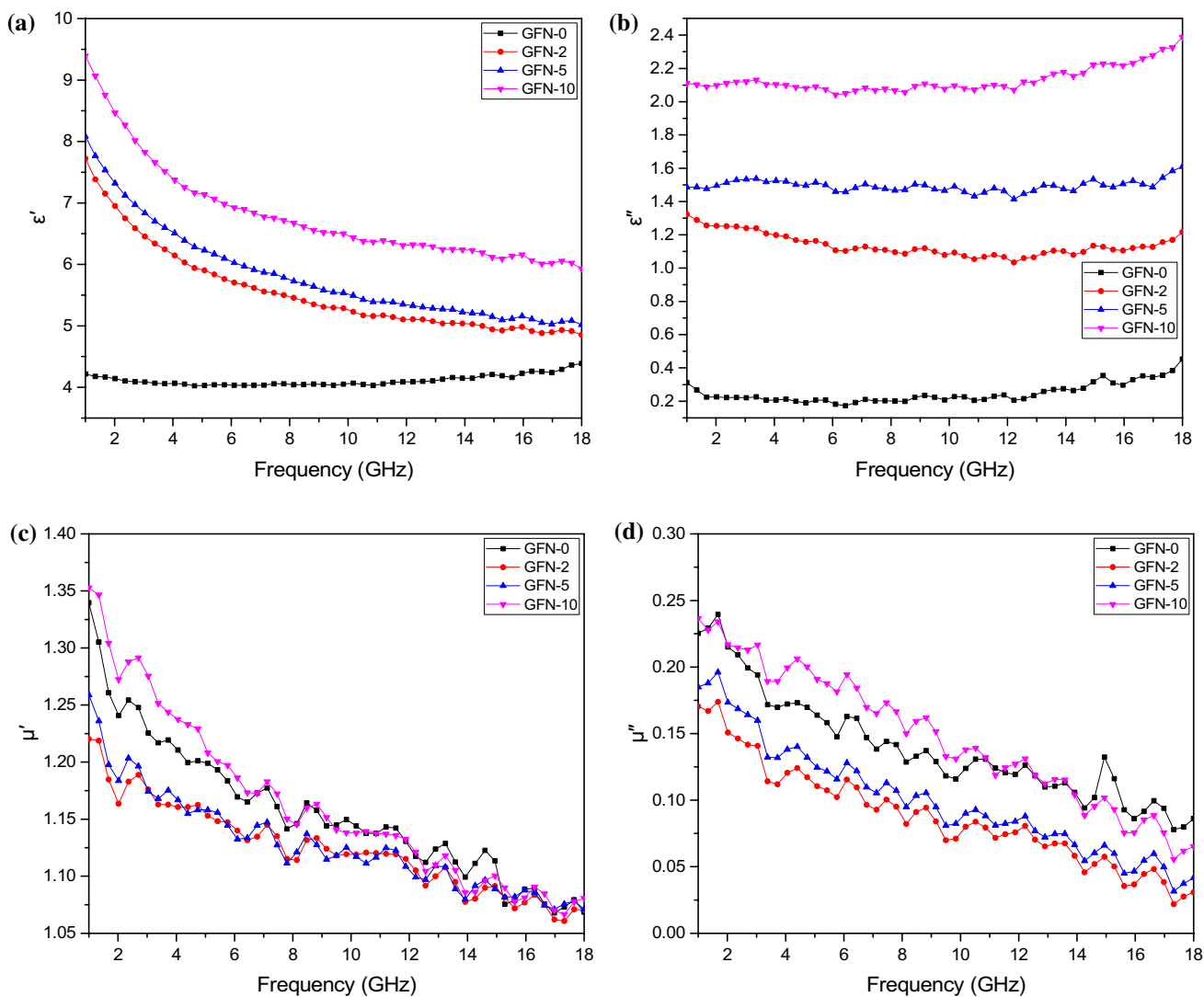


Fig. 5 **a** The real and **b** imaginary parts of the permittivity; **c** the real and **d** imaginary parts of the permeability of the composites

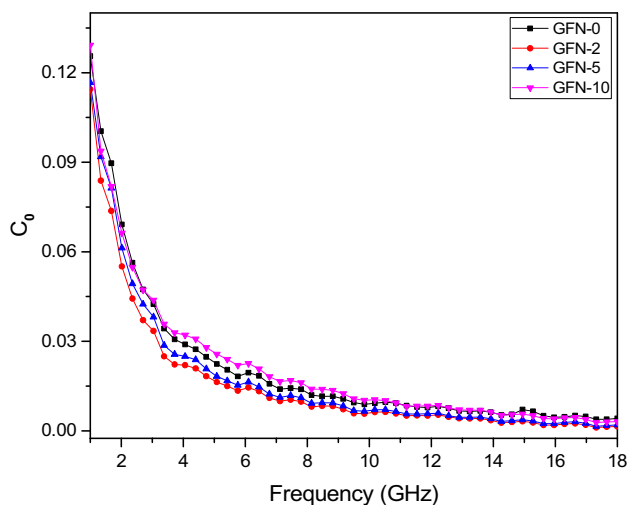


Fig. 6 Q_0 - f curves of Fe@Ni/epoxy and GFN/epoxy composites

absorption properties. As layer thickness increases, the absorption peaks gradually shift to lower frequency. The peak values of GFN-0 samples are at about -6 dB, far away from the effective absorption intensity. On the contrary, the minimal RL values of GFN-2 and GFN-5 samples are -9.8 and -13.6 dB respectively, higher than those of GFN-0 samples. Especially for GFN-10 samples in Fig. 7d, the higher RL value means enhanced microwave absorption performance, even though they have a same amount of Fe@Ni NPs. It's worth noting that GFN-10 samples show an optimal absorption peak reaching up to -22.7 dB at 14.9 GHz and the corresponding absorption bandwidth at RL exceeding -10 dB is approximately 5.5 GHz from 12.5 to 18 GHz. In addition, GFN-10 samples exhibit about 1 GHz (14.6–15.6 GHz) strong absorption bandwidth with $RL \leq -20$ dB. As is known to all, RL value at -20 dB corresponds to 99% attenuation of incident microwave, signifying more effective absorption in practical applications. Thus,

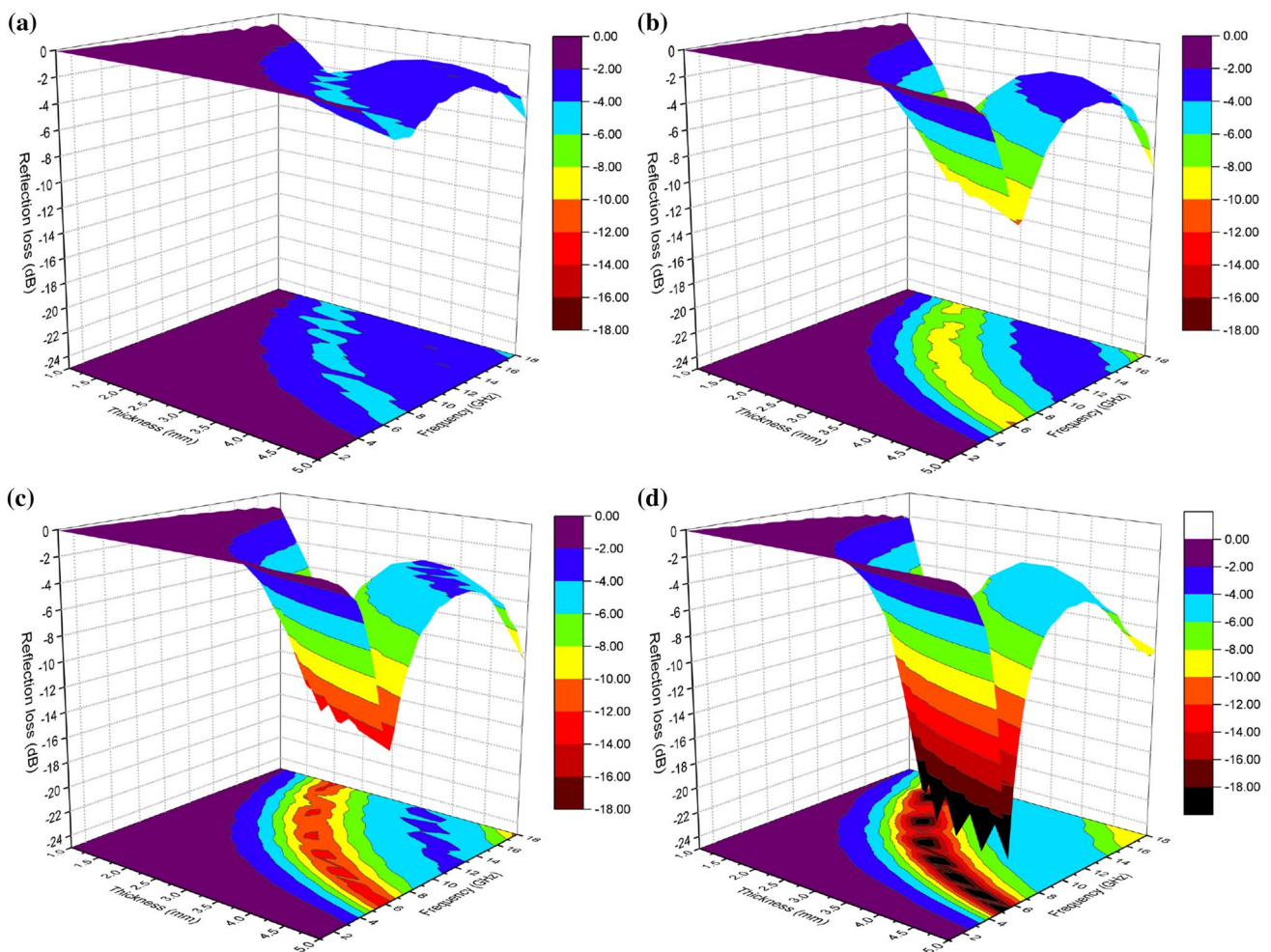


Fig. 7 3D-colormap RL values of **a** GFN-0, **b** GFN-2, **c** GFN-5, **d** GFN-10 samples

GFN-10 composites possess the best microwave absorption performance among all the prepared absorbers in this work. Furthermore, focusing on the projection map at the bottom of each 3D-colormap, the RL peaks move to low frequency with the increasing matching thickness. This phenomenon is in accordance with the following formula $f_m = c/2\pi\mu''d$ [42], where f_m is frequency of maximum RL peak and d is matching thickness.

As previous stated, the enhanced RL values of GFN-10 samples is mainly attributed to two key factors: better impedance matching condition and enhanced microwave attenuation. Firstly, the direct reflection should be minimum so that microwave as much as possible can propagate into the interior. Reflection coefficient Γ is generally adopted to evaluated it below [43]:

$$\Gamma = \frac{Z_{in} - Z_0}{Z_{in} + Z_0} \quad (4)$$

In order to achieve impedance match, i.e., zero reflection condition, the input impedance Z_{in} should equal free-space characteristic impedance Z_0 (377 Ω). According to Eq. (2), the imaginary part Z_{in}'' approaches 0 Ω , while the corresponding real part Z_{in}' gets close to 377 Ω simultaneously. Figure 8 shows the complex impedance of Fe@Ni/epoxy and GFN/epoxy composites. It's apparent that GFN-10 samples have the best impedance matching condition at 14.9 GHz, the corresponding Z_{in}'' and Z_{in}' is -15.9 and 434.1 Ω respectively. Whereas for GFN-0, GFN-2 and GFN-5 samples, the corresponding Z_{in}'' and Z_{in}' are away from the free-space characteristic impedance, especially those GFN-0 samples show conspicuous impedance mismatch. Nothing but magnetic or dielectric loss materials result in a poor impedance match and the combination of dielectric RGO sheets and magnetic Fe@Ni NPs have been proved to be a efficient route to achieve better impedance matching condition.

Secondly, the incident microwave energy should be fleetly and entirely dissipated inside the absorbers. In order to quantitatively evaluate the microwave attenuation performance

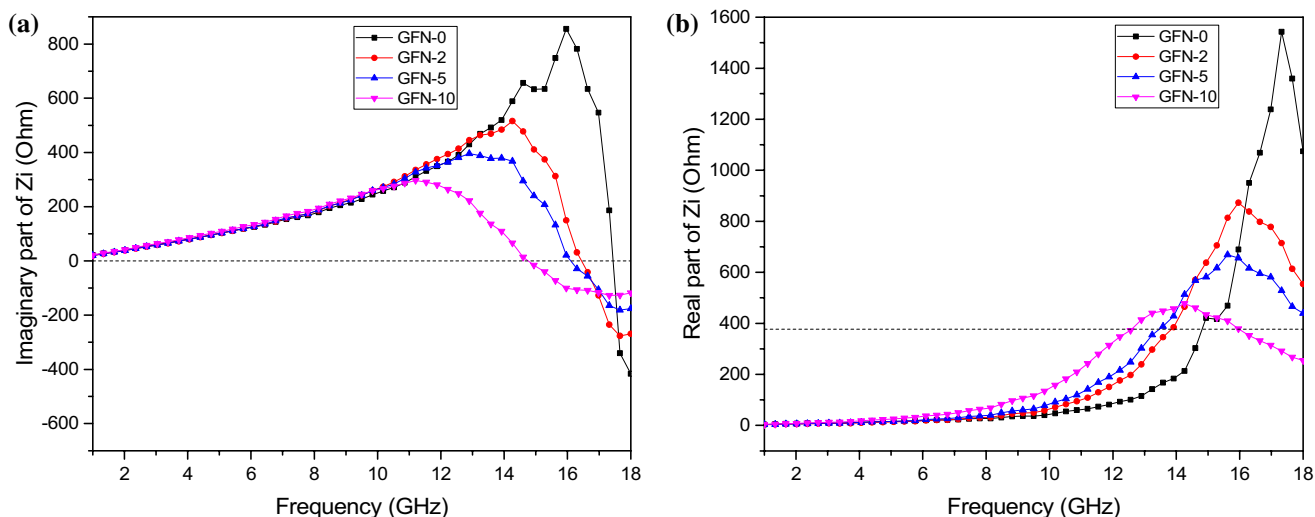


Fig. 8 Complex impedance of the composites: **a** imaginary part and **b** real part

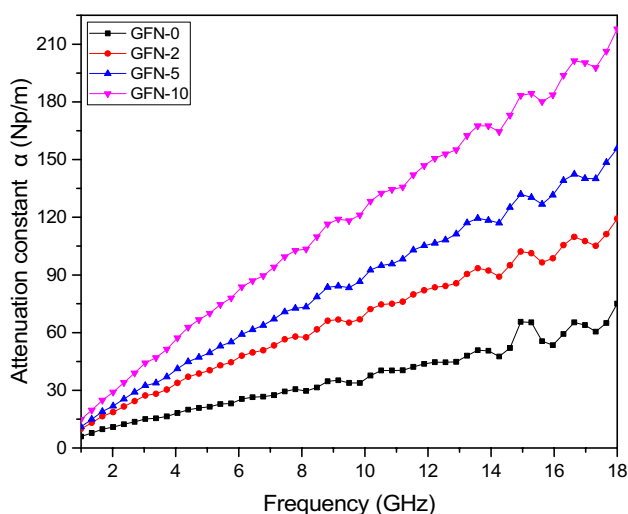


Fig. 9 Attenuation constant α of the composites

of those absorbers, attenuation constant α is introduced and calculated by following equation [44]:

$$\alpha = \frac{\pi f}{c} \left(2 \left(\mu'' \epsilon'' - \mu' \epsilon' + \left((\mu'^2 + \mu''^2)(\epsilon'^2 + \epsilon''^2) \right)^{1/2} \right) \right)^{1/2} \quad (5)$$

Figure 9 exhibits the attenuation constant of Fe@Ni/epoxy and GFN/epoxy composites. It's apparent that GFN-10 samples exhibit a biggest α than other samples in all frequency range, indicating GFN-10 samples possess excellent attenuation or microwave absorption. It can be inferred from Eq. (5) that high values of ϵ'' and μ'' are beneficial for high α . As mentioned above, the highest ϵ'' is related to interfacial polarization and relaxation. The multi-interfaces and defects in GFN/epoxy composites induce polarization

centers, which result in stronger dielectric loss. Moreover, the advanced conductive networks formed by RGO sheets and adopted metallic Fe@Ni NPs lengthen the propagation path of incident EM wave due to multiple reflection, leading to more energy dissipation [45, 46]. By optimizing the ratio of RGO and Fe@Ni NPs, best impedance matching and microwave attenuation can be obtained, so is a promising high performance microwave absorber.

4 Conclusions

In summary, core-shell metallic magnetic Fe@Ni decorated RGO/epoxy composites with enhanced microwave absorption performance have been successfully prepared via a two-step method. Fe@Ni NPs dispersed homogeneously on both sides of RGO sheets, preventing RGO sheets from aggregating and forming advanced conductive networks. The complementary effects between magnetic Fe@Ni NPs and dielectric RGO sheets generate better impedance match and enhanced microwave attenuation ability. Compared with Fe@Ni/epoxy composites, the GFN/epoxy composites show stronger microwave absorption performance. With a loading of 1 wt% RGO and 10 wt% Fe@Ni, the minimum value of RL can reach up to -22.7 dB at 14.9 GHz with a layer thickness of 2 mm, and the widest absorption bandwidth exceeding -10 dB is about 5.5 GHz. The calculated RL values and lightweight feature of Fe@Ni/RGO demonstrate the as-synthesized composites could be potential candidates in microwave absorption application.

Acknowledgements This work is supported by the National Natural Science Foundation of China (Grant Nos. 51373129 and 51672201) and the Fundamental Research Funds for the Central Universities

(WUT 2017-YB-006). The authors acknowledge the help of Rongguo Song (School of Science, Wuhan University of Technology) for EM measurements.

References

1. Y.C. Qing, W.C. Zhou, F. Luo, D.M. Zhu, *Ceram. Int.* **42**, 16412 (2016)
2. X. Li, B. Zhang, C. Ju, X. Han, Y. Du, P. Xu, *J. Phys. Chem. C* **115**, 12350 (2011)
3. X.F. Zhang, H. Huang, X.L. Dong, *J. Phys. Chem. C* **117**, 8563 (2013)
4. Y. Wang, H. Zhu, Y. Chen, X. Wu, W. Zhang, C. Luo, J. Li, *Mater. Chem. Phys.* **202**, 184 (2017)
5. Q. Yuchang, W. Qinlong, L. Fa, Z. Wancheng, Z. Dongmei, *J. Mater. Chem. C* **4**, 371 (2016)
6. J. Li, W.J. Feng, J.S. Wang, X. Zhao, W.Q. Zheng, H. Yang, *J. Magn. Magn. Mater.* **393**, 82 (2015)
7. K. Ali, J. Iqbal, T. Jana, N. Ahmad, I. Ahmad, D. Wan, *J. Alloys Compd.* **696**, 711 (2017)
8. F. Qin, C. Brosseau, *J. Appl. Phys.* **111**, 061301 (2012)
9. X. Chen, J. Chen, F. Meng, L. Shan, M. Jiang, X. Xu, J. Lu, Y. Wang, Z. Zhou, *Compos. Sci. Technol.* **127**, 71 (2016)
10. J.C. Apesteguy, A. Damiani, D. DiGiovanni, S.E. Jacobo, *Physica B* **407**, 3168 (2012)
11. X. Tang, Q. Tian, B. Zhao, K. Hu, *Mater. Sci. Eng. A* **445–446**, 135 (2007)
12. Y. Feng, T. Qiu, *J. Alloys Compd.* **513**, 455 (2012)
13. S.L. Wen, Y. Liu, X.C. Zhao, Z.Z. Fan, *J. Magn. Magn. Mater.* **385**, 182 (2015)
14. X.F. Zhang, X.L. Dong, H. Huang, Y.Y. Liu, W.N. Wang, X.G. Zhu, B. Lv, J.P. Lei, C.G. Lee, *Appl. Phys. Lett.* **89**, 053115 (2006)
15. Y. Wang, X. Wu, W. Zhang, C. Luo, J. Li, Q. Wang, *Synth. Met.* **231**, 7 (2017)
16. F. Akbar, M. Kolahdouz, S. Larimian, B. Radfar, H.H. Radamson, *J. Mater. Sci.-Mater. Electron.* **26**, 4347 (2015)
17. Q. Yuchang, W. Qinlong, L. Fa, Z. Wancheng, *J. Mater. Chem. C* **4**, 4853 (2016)
18. H. Xian, T. Peng, H. Sun, J. Wang, *J. Mater. Sci.: Mater. Electron.* **26**, 242 (2015)
19. C. Wang, X. Han, P. Xu, X. Zhang, Y. Du, S. Hu, J. Wang, X. Wang, *Appl. Phys. Lett.* **98**, 072906 (2011)
20. Y. Zhang, Y. Huang, T. Zhang, H. Chang, P. Xiao, H. Chen, Z. Huang, Y. Chen, *Adv Mater* **27**, 2049 (2015)
21. J. Wang, J. Wang, R. Xu, Y. Sun, B. Zhang, W. Chen, T. Wang, S. Yang, *J. Alloys Compd.* **653**, 14 (2015)
22. Z. Zhu, X. Sun, G. Li, H. Xue, H. Guo, X. Fan, X. Pan, J. He, *J. Magn. Magn. Mater.* **377**, 95 (2015)
23. G. Wang, L. Wang, Y. Gan, W. Lu, *Appl. Surf. Sci.* **276**, 744 (2013)
24. C. Bao, L. Song, W. Xing, B. Yuan, C.A. Wilkie, J. Huang, Y. Guo, Y. Hu, *J. Mater. Chem.* **22**, 6088 (2012)
25. I.K. Moon, J. Lee, R.S. Ruoff, H. Lee, *Nat. Commun.* **1**, 73 (2010)
26. A. Arora, S.B. Narang, K. Pubby, *J. Magn. Magn. Mater.* **423**, 441 (2017)
27. J. Liu, Y. Feng, T. Qiu, *J. Magn. Magn. Mater.* **323**, 3071 (2011)
28. X.L. Dong, Z.D. Zhang, X.G. Zhao, Y.C. Chuang, S.R. Jin, W.M. Sun, *J. Mater. Res.* **14**, 398 (2011)
29. B. Zhang, J. Wang, J. Wang, H. Duan, S. Huo, Y. Tang, *J. Mater. Sci.: Mater. Electron.* **28**, 3337 (2016)
30. B. Zhang, J. Wang, J. Wang, S. Huo, B. Zhang, Y. Tang, *J. Magn. Magn. Mater.* **413**, 81 (2016)
31. B. Lu, H. Huang, X.L. Dong, X.F. Zhang, J.P. Lei, J.P. Sun, C. Dong, *J. Appl. Phys.* **104**, 114313 (2008)
32. W. Li, T. Qiu, L. Wang, S. Ren, J. Zhang, L. He, X. Li, *ACS Appl. Mater. Interfaces* **5**, 883 (2013)
33. S. Zhou, Q. Zhang, H. Liu, X. Gong, J. Huang, *Mater. Chem. Phys.* **134**, 224 (2012)
34. Y. Qing, H. Nan, F. Luo, W. Zhou, *RSC Adv.* **7**, 27755 (2017)
35. C. Feng, X. Liu, Y. Sun, C. Jin, Y. Lv, *RSC Adv.* **4**, 22710 (2014)
36. D. Han, S.W. Or, X. Dong, B. Liu, *J. Alloys Compd.* **695**, 2605 (2017)
37. Y. Wang, H. Guan, C. Dong, X. Xiao, S. Du, Y. Wang, *Ceram. Int.* **42**, 936 (2016)
38. X.G. Liu, D.Y. Geng, H. Meng, P.J. Shang, Z.D. Zhang, *Appl. Phys. Lett.* **92**, 173117 (2008)
39. B. Zhang, J. Wang, X. Su, H. Duan, H. Cai, J. Wang, S. Yang, S. Huo, *J. Mater. Sci.: Mater. Electron.* **28**, 12122 (2017)
40. Y. Pang, X. Xie, D. Li, W. Chou, T. Liu, *J. Magn. Magn. Mater.* **426**, 211 (2017)
41. Y. Wang, X.M. Wu, W.Z. Zhang, *Mater. Lett.* **165**, 71 (2016)
42. J. Luo, P. Shen, W. Yao, C. Jiang, J. Xu, *Nanoscale Res. Lett.* **11**, 141 (2016)
43. G.Z. Shen, Y.W. Xu, B. Liu, P. Du, Y. Li, J. Zhu, D. Zhang, *J. Alloys Compd.* **680**, 553 (2016)
44. M.S.S. Dorraji, M.H. Rasoulifard, M.H. Khodabandelloo, M. Rastgouy-Houjaghan, H.K. Zarajabad, *Appl. Surf. Sci.* **366**, 210 (2016)
45. M. Qiao, X. Lei, Y. Ma, L. Tian, W. Wang, K. Su, Q. Zhang, *J. Alloys Compd.* **693**, 432 (2017)
46. Y. Wang, Y. Fu, X. Wu, W. Zhang, Q. Wang, J. Li, *Ceram. Int.* **43**, 11367 (2017)